Quantifying the impact of bedrock topography uncertainty in Pine Island Glacier projections for this century*

Andreas Wernecke[1,2,3], Tamsin L. Edwards[4], Philip B. Holden[1], Neil R. Edwards[1], Stephen L. Cornford [5]

[1]School of Environment, Earth and Ecosystem Sciences, The Open University, Milton Keynes, UK
[2]Max-Planck-Institute for Meteorology, Hamburg, Germany
[3]Universität Hamburg, Hamburg, Germany
[4]Kings Collage London, London, UK
[5]Faculty of Science and Engineering, Swansea University, Swansea, UK

Key Points:

- Uncertainty in topography estimates has a significant impact on predictions for all tested friction laws
- Simulations with BedMachine and statistically generated topographies are more sensitive to upper-end climate forcing than with Bedmap2
- Pine Island Glacier is likely to transition into a more unstable state late mid-century for upper-end climate forcing

*accepted author manuscript

Corresponding author: Andreas Wernecke, andreas.wernecke@mpimet.mpg.de

Abstract

The predicted Antarctic contribution to global-mean sea-level rise is one of the most uncertain among all major sources. Partly this is because of instability mechanisms of the ice flow over deep basins. Errors in bedrock topography can substantially impact the projected resilience of glaciers against such instabilities. Here we analyze the Pine Island Glacier topography to derive a statistical model representation. Our model allows for inhomogeneous and spatially dependent uncertainties and avoids unnecessary smoothing from spatial averaging or interpolation. A set of topography realizations is generated representing our best estimate of the topographic uncertainty in ice sheet model simulations. The bedrock uncertainty alone creates a 5% to 25% uncertainty in the predicted sea level rise contribution at year 2100, depending on friction law and climate forcing. Pine Island Glacier simulations on this new set are consistent with simulations on the BedMachine reference topography but diverge from Bedmap2 simulations.

Plain Language Summary

We investigate the impact of uncertainties in the elevation of the bedrock underneath the ice of a particularly vulnerable glacier in Antarctica. We propose a new approach to better estimate how much future projections depend on knowledge of bedrock elevation. The main focus of this study is to represent the current understanding of the bedrock elevation as closely as possible so that our simulations accurately reflect the extent of our knowledge of the future glacier behaviour. In summary, we find that the mass of ice lost in simulations for year 2100, which contributes to the global mean sea level, can be affected by up to 25%. This highlights the value of closely-spaced bedrock measurement and of careful consideration of related uncertainties in ice-sheet simulations.

1 Introduction

The Antarctic ice sheet is one of the major sources of global sea level rise and is currently losing mass at a rate of 0.5 to 0.6 mm global mean Sea Level Equivalent per year (mm SLE a^{-1}), predominantly in the Amundsen Sea Embayment (ASE) area of the West Antarctic Ice Sheet (WAIS) (Shepherd et al., 2018; Bamber et al., 2018). The future response of the Antarctic ice sheet to a changing climate is one of the least well understood aspects of climate predictions (Oppenheimer et al., 2019).

Changes in the Antarctic ice sheet mass balance are largely governed by changes in the Surface Mass Balance (SMB) and ocean forcing via dynamical processes such as changing buttressing from ice shelves. Ice shelves, the floating extensions of grounded ice streams, can be weakened by elevated ocean or atmospheric temperatures and subsequent melt or collapse. Buttressing ice shelves have a stabilising effect on the ice sheet with the potential to suppress or delay Marine Ice Sheet Instability (MISI) (Schoof, 2007; Joughin & Alley, 2011). MISI can occur at ice sheets on retrograde topographies below sea level. Here a retreat of the Grounding Line (GL), the transition from grounded to floating ice, corresponds to a migration below thicker ice. For idealised conditions the mass flux across the GL increases rapidly with the ice thickness above it (Schoof, 2007). This additional mass loss can lead to an imbalance of the system causing a thinning of the ice upstream, which facilitates further GL retreat below even thicker ice. Large areas of the WAIS, including the ASE, lie on such retrograde topography (Fretwell et al., 2013). Pine Island Glacier (PIG), one of two major glacial systems of the ASE, has a large drainage basin and shares an ice divide with the Ronne-Filchner ice shelf drainage basin, so that a sustained thinning of PIG could ultimately influence most of the WAIS.

In the satellite record the ASE shows significant rates of thinning (Rignot et al., 2008; Mouginot et al., 2014; Shepherd et al., 2018), which have been linked to warm Circumpolar Deep Water entering the continental shelf (Dutrieux et al., 2014; Naughten et al., 2018; Rignot et al., 2014). Additional oceanic heat transport to the continent causes enhanced ocean melt which can thin and weaken the buttressing ice shelves. This might have caused a GL retreat and triggered Marine Ice Sheet Instability in the ASE at present (Joughin et al., 2014; Favier et al., 2014; Alley et al., 2015). Bamber and Dawson (2020) find a recent reduction of rates of mass loss from PIG even though it has maintained a negative mass balance and elevated flow speeds. This behaviour could be related to lower ocean temperatures in 2012-2013 compared with the 2000s (Milillo et al., 2017). In summary, PIG currently loses mass, shows strong sensitivity to ocean conditions and is situated on a bedrock topography which makes it vulnerable to instability.

Predictions of the dynamic ice sheet response are challenging because of poorly observed local ice properties and the bedrock underneath, including the bedrock elevation, which suffer from measurement and spatial interpolation errors. As described, MISI depends on the local topography; a regional sill along the GL can create a stable resting point for an otherwise unstable ice stream. This kind of topographic feature can be concealed even if the large-scale geometry is well represented, for example due to insufficient sampling density (Durand et al., 2011).

Several studies highlight the importance of the bedrock topography. Zhao et al. (2018) show that it influences the model inversion for basal traction coefficients. The impact of these results on forward simulations is, however, not investigated. The differences between Bedmap2 and its predecessor Bedmap1 can exceed the uncertainty in Antarctic sea level rise contribution from surface accumulation, melt rate, basal friction and ice viscosity combined (Schlegel et al., 2018). Consistent findings are reported by Nias et al. (2016, 2018). In order to investigate the impact of the topography uncertainty, random noise is imposed repeatedly on a reference topography in Sun et al. (2014) and Gasson et al. (2015). In 3000-year ice sheet simulations of the mid-Pliocene the sea level contribution can vary by more than 5 m global SLE (from 12.6 m to 17.9 m SLE) (Gasson et al., 2015). Sun et al. (2014) show with a similar approach that the sensitivity of modern ice sheet simulations to topographic uncertainty is much stronger for a longer correlation length (50 km) than for shorter values (5 to 10 km). This is despite equal noise amplitude and power spectral density which means that uncorrelated errors in the bedrock topography (e.g. from radar measurement noise) are less of a concern for ice sheet simulations than spatially correlated errors (e.g. from interpolation over large distances). Sun et al. (2014) also note that a topographic ridge near the PIG GL has a strong impact on the GL retreat if lowered or raised by only tens of metres but do not assess whether these kinds of larger spatial-scale errors in the topography are likely. Furthermore, the noise amplitude is solely based on the Bedmap2 uncertainty estimate so that the measurement locations are not directly taken into account.

We here move beyond randomised sensitivity studies to generate a statistical description of the current observational knowledge of the bedrock topography, creating an ensemble of representative topographies that are all consistent with these observations. We apply the ensemble to idealised but plausible forcing scenarios to quantify the uncertainty in sea level rise contribution predictions, arising from observational uncertainties in the PIG topography.

We introduce the airborne radar measurements used here and analyse the geostatistical properties in Section 2. Based on this we set up simulations of the ice sheet model BISICLES in Section 3. This includes the statistical generation of a set of bedrock topographies which are in agreement with observational constraints while aiming to fully represent their uncertainties. Section 3 further describes the initialisation

and parameter inversion of the ice sheet model BISICLES, followed by a description of three friction laws and two climate forcings for the PIG simulations. Results are presented in Section 4 with focus on the sea level rise contribution uncertainty. Finally we discuss how bedrock uncertainty translates into predictive uncertainty in Section 5.

2 Data and Methods

We summarize our knowledge of the real bedrock in a multivariate random variable which is approximated by a Gaussian Process (GP). This statistical model can sample spatial fields of bedrock topography with local uncertainties and spatial covariance structure to represent measurement and interpolation uncertainties. To define a GP model, training data and covariance function parameters are required (Rasmussen & Williams, 2006). Ungridded airborne radar measurements are analysed to estimate the statistical characteristics of the bedrock topography observations. This provides us with the required GP model covariance function parameters. We train the GP to match observed values, given the observational uncertainty, and draw random samples to make the handling of topography uncertainty feasible for the ice sheet model BISICLES.

The airborne Radar Echo Sounding (RES) dataset used here is a union of two different collections, namely the one described in Holt, Blankenship, Morse, et al. (2006), and Operation Ice Bridge IRMCR2 Level-2 data from October 2009 to December 2017 (Paden et al., 2010). This combined collection consists of about 2.3 million ungridded radar measurements from the grounded PIG catchment area, as defined in Mouginot et al. (2017) based on Rignot et al. (2013). About 1.5% of these measurements are removed here by manual inspection due to inconsistencies (Text S1 and Figure S1 in the Supplement). For training the statistical model the RES dataset is sub-sampled for computational reasons. This is done by imposing a 2 km $\times$ 2 km grid onto the region and randomly selecting one measurement from each box from the combined measurement collection (giving about 25 000 measurements in total). This ensures a good spatial coverage while avoiding smoothing effects from averaging. The covariance function is derived from semivariograms on fully random subsets of 100 000 measurements without restriction on the proximity of sample points. Exponential functions are fitted to the semi-variance on scales of 25 km to 50 km to derive the uncorrelated uncertainty (σ_n^2), correlation length scale (ℓ) and far-field semivariance, or sill, (σ_c^2) to describe the spatial correlation characteristics. The uncorrelated uncertainty is an estimate of the uncertainty of two measurements at the same location and represents the measurement uncertainty, including uncertainties from sub-resolution variability, while a larger correlation length of the topography simplifies any interpolation and reduces the corresponding uncertainty. The far-field semivariance describes the amplitude of variations in the topography field. These exponential fits accurately capture the semivariance (Figure S2 in the Supplement) which motivates our use of an exponential covariance function c_E for the GP, defined as:

$$COV(x_i, x_j) = c_E(r, \sigma_c^2, \ell, \sigma_n^2) = \sigma_c^2 \exp\Big(-\frac{r}{2\ell}\Big) + \sigma_n^2 \cdot \delta_{ij},$$

where $COV(x_i.x_j)$ is the covariance in the bedrock topography at the locations x_i and x_j, r is the physical distance between the locations x_i and x_j and δ_{ij} is the Kronecker delta which is one if $i = j$ and zero otherwise. The randomized sub-sampling for deriving the covariance parameters and the training data is repeated to capture the impact on the final simulations. See Text S2 in the Supplement for more information.

We generate random two-dimensional sample fields which adhere to the full spatial covariance matrix and the local observational uncertainties, as illustrated in Figure 1a. The topographic uncertainty increases with distance to the closest measure-

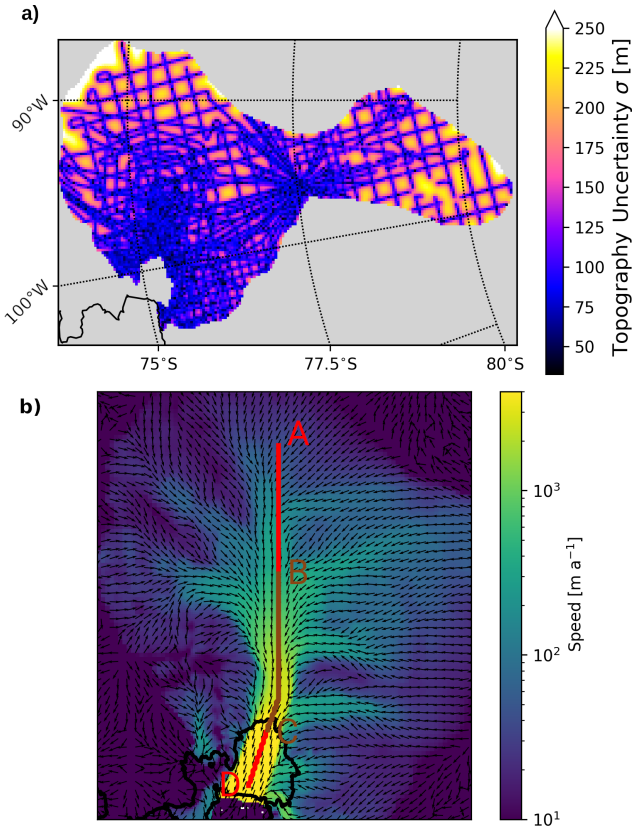

Figure 1. a: One standard deviation of trained GP which increases with distance from measurements (flight lines) and b: Initial PIG ice velocity direction (arrows) and speed (colours), for the main trunk (left half of panel a) of PIG flow including the approximate central flow line (red and brown).

ment (flight line) and is often above 50 m (one standard deviation), even in regions with close sampling.

The computational demand of sampling from a GP scales with the number of evaluated grid cells n by $\mathcal{O}(n^3)$, which imposes a limit on this number. We use the Python GPy module to draw 12 samples on a 4 km×4 km grid in the PIG catchment area. The statistically generated bedrock topographies within the grounded PIG catchment area are solely based on RES measurements and statistical modelling. However, we use Bedmap2 topography and ice thickness outside of the grounded catchment area, brought to the same resolution by averaging. This includes all locations of the Bedmap2 ice shelf mask.

The ice surface elevation is considered well known and the ice thickness is adjusted for all statistically generated topographies to match the Bedmap2 surface elevation. The resulting 12 topographies are accompanied by the Bedmap2 (Fretwell et al., 2013) and BedMachine (Morlighem, 2019; Morlighem et al., 2020) reference topographies with the same resolution.

3 Simulations

We use all combinations of the 14 topographies described above with three friction laws and two climate forcings, resulting in a total of 84 simulations. The simulations are performed by the ice sheet model BISICLES (Cornford et al., 2013, 2015), which is a finite-volume model with vertically integrated stress approximations. BISICLES combines the L1L2 approximation (Schoof & Hindmarsh, 2010) with an adaptive mesh refinement which allows for fine spatial resolutions near the GL and in fast flowing ice streams, and lower resolutions where the flow is slower and more homogeneous. The finest resolution used here is 500 m. The BISICLES inverse model framework (Cornford et al., 2015, Appendix B1) is used with a compilation of satellite based ice surface velocities from Rignot et al. (2017, 2011) to find basal traction coefficient and effective viscosity fields for each individual topography (Text S3 in the Supplement). The basal traction coefficient, effective viscosity and topography fields do not evolve over time. Figure 1b illustrates the initial velocity field of the main PIG trunk.

The Weertman friction law is :

$$\tau_b = C_m \cdot |u_b|^{m-1} \cdot u_b$$

with τ_b being the basal stress tangential to the base of the ice, C_m is the spatially varying basal traction coefficient for a given friction law exponent m and u_b is the basal ice velocity. We use $m = 1$ for linear friction, $m = 1/3$ for nonlinear friction and $m = 1/8$ for strongly nonlinear friction (called plastic friction in the following, see also Joughin et al. (2019)). Ice flow outside of the PIG catchment area is suppressed for numerical stability.

3.1 Climate forcing

We use two different climate forcings with changing ocean melt and SMB. These two forcings are intended to encompass the range of likely climate scenarios:

1. The **low forcing** uses an RCP2.6 SMB and constant-in-time ocean melt rates.
2. The **high forcing** uses an RCP8.5 SMB and linearly increasing ocean melt, starting at the low forcing rates and adding 200 % by the end of the 100-year model simulations

As SMB we use yearly output directly from NorESM1-M, a CMIP5 atmosphere-ocean coupled global climate model (Bentsen et al., 2013). Of the three models se-

lected in Barthel et al. (2020) for the ice sheet model intercomparison project ISMIP6 (Seroussi et al., 2020), NorESM1-M has the highest rank in the CMIP5 cross-model performance analysis by Agosta et al. (2015). The simulations show below median atmospheric warming and relatively strong 21st century ocean warming compared with the multi-model ensemble (Barthel et al., 2020). The ocean melt at the beginning of the simulations is based on temperature and salinity profiles corresponding to the Warm_0 setup in Favier et al. (2019) which is based on oceanographic measurements from Dutrieux et al. (2014). We use an ocean melt parameterisation with a quadratic dependence on the local ocean temperature above freezing, as defined in Favier et al. (2019) as M_{quad}. The squared dependency represents a positive feedback between subshelf melting and the circulation in the cavity and this parameterisation reproduces results from coupled ocean-ice sheet model simulations relatively well (Favier et al., 2019).

Predictions of future ocean melt forcing are highly uncertain, but cannot be ignored for century-scale model simulations. The two forcings used here are designed to represent reasonable low and high melt scenarios without being bound to specific climate projections. Naughten et al. (2018) analyse and select CMIP5 model output as forcing for the regional ocean model FESOM. The ocean model predicts a year 2100 ASE ocean melt increase of about 200% (multi-model mean) to 300% (ACCESS-1.0) for RCP8.5. However, the warming should be seen largely as reversal of a known model bias which makes it very likely that the increase in melt is overestimated (Naughten et al., 2018). This overestimation might be up to about 150% in melt increase (Wernecke, 2020, Section 5.2.3). We select an increase of 200% in 100 years as a best guess upper-end melt representation. It cannot be ruled out that current ocean conditions are a positive anomaly caused by internal variability. Climate projections of ice shelf ocean melt rates for the ASE often show positive trends (Naughten et al., 2018; Alevropoulos-Borrill et al., 2020; Jourdain et al., 2020), but some projections show temporarily negative ocean temperature anomalies compared to the early 2000s (Jourdain et al., 2020; Alevropoulos-Borrill et al., 2020). We apply a constant ocean melt forcing, consistent with recent past rates, as reasonable lower-end forcing.

4 Results

4.1 Simulations

In the first years we see high-amplitude small spatial-scale rates of ice thickness change which diminish over time. This is an adjustment of the model to a self-consistent state. In retrospect we should have implemented a spin-up period in the simulations with a constant forcing before the forced projections start. Instead our simulations start with forcing, including SMB corresponding to year 2000 AD. After 15 years of simulation, corresponding to 2015 AD, the initial model adjustment becomes negligible (Text S4 and figures S3 and S4 in the Supplement), hence we choose to make all following calculations relative to the state in 2015. In this way the impact of initial adjustments on the results is minimized.

The ice geometry and flow speed along the downstream sector of the central PIG flow line (B to D in Figure 1b) is illustrated for plastic friction in Figure 2. The statistically generated topographies (right) show more variability than Bedmap2 and BedMachine (left). For low forcing the glacier thins slightly without much change of the GL position. At the same time the ice speed reduces, in particular in the fast-flowing ice shelf. A partial slowdown of the PIG is also predicted for the flow line model simulations in Gladstone et al. (2012) and is found in the optimized (central) simulations from Nias et al. (2016) for all combinations of bedrock and friction law (not shown).

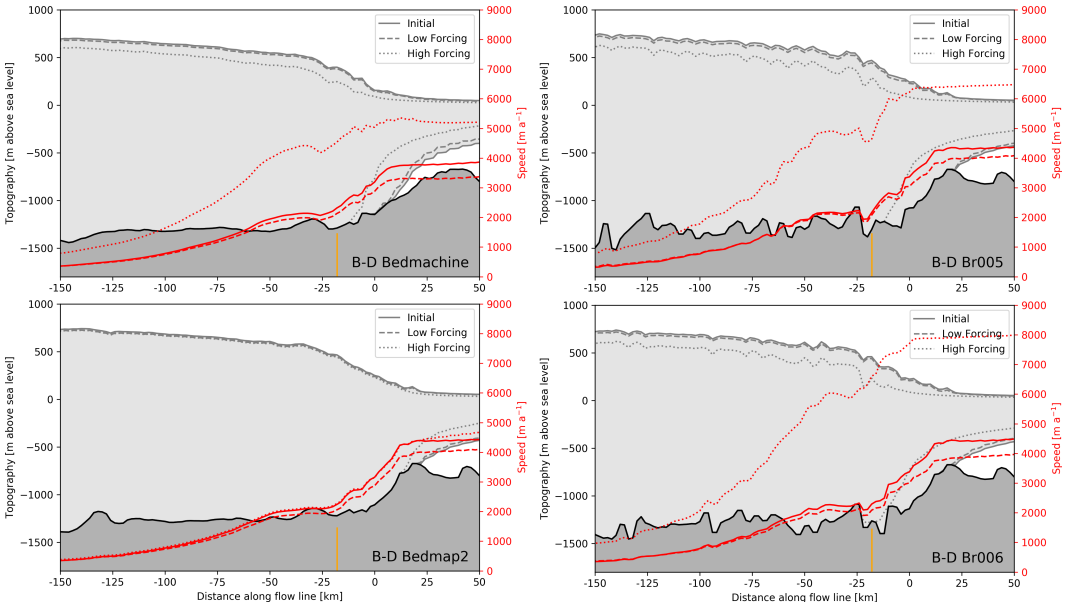

Figure 2. Profiles along PIG flow line from location B to D in Figure 1, relative to the BedMachine GL with BedMachine (top left) and Bedmap2 (bottom left) and two statistically generated topographies (right). Shown are the bedrock underneath the ice (black), surface and basal ice boundaries (grey) and the ice speed (red) after 15 years of simulation (used as baseline; solid lines) and at the end of the 100-year simulations with high (dotted) and low (dashed) forcing, all using the plastic friction law. The orange line highlights a location where Bedmap2 lies above all statistically generated topographies and BedMachine.

For the high forcing scenario we see very different pictures for BedMachine and Bedmap2 geometries: For BedMachine the ice near its GL accelerates over the 85 year projection period from less than 4000 m a^{-1} to more than 5000 m a^{-1}. The speed-up extends more than 150 km upstream (red lines in Figure 2). For Bedmap2 the high forcing scenario does not show noteworthy acceleration or thinning.

The flow line characteristics of two topographies generated here are shown on the right of Figure 2. Simulations with statistically generated topographies share the same features of those using BedMachine: little changes to the ice geometry with some slowdown of the ice for low forcing, and pronounced thinning with significant retreat of their GLs and accelerating ice for high forcing.

4.2 Sea level rise contribution

The ensemble behaviour can be categorized into two states, a steadily evolving state with approximately constant rates of mass loss (about 0.1 mm SLE a^{-1}) and an unstable state with mass losses up to six times higher (Figure 3, top). The timing of an ensemble member to become unstable depends strongly on the topography and forcing: most high melt simulation become unstable between 2055 and 2075. This timing seems not to depend on the friction law (Figure 3, top right). Low melt ensemble members remain in the steadily evolving state without exception.

The main effect of the friction law is an increase in the rate of mass loss in the unstable state with higher rates for more non-linear friction laws (Figure 3, middle). For low forcing the relationship is reversed, more linear friction leads to larger sea level

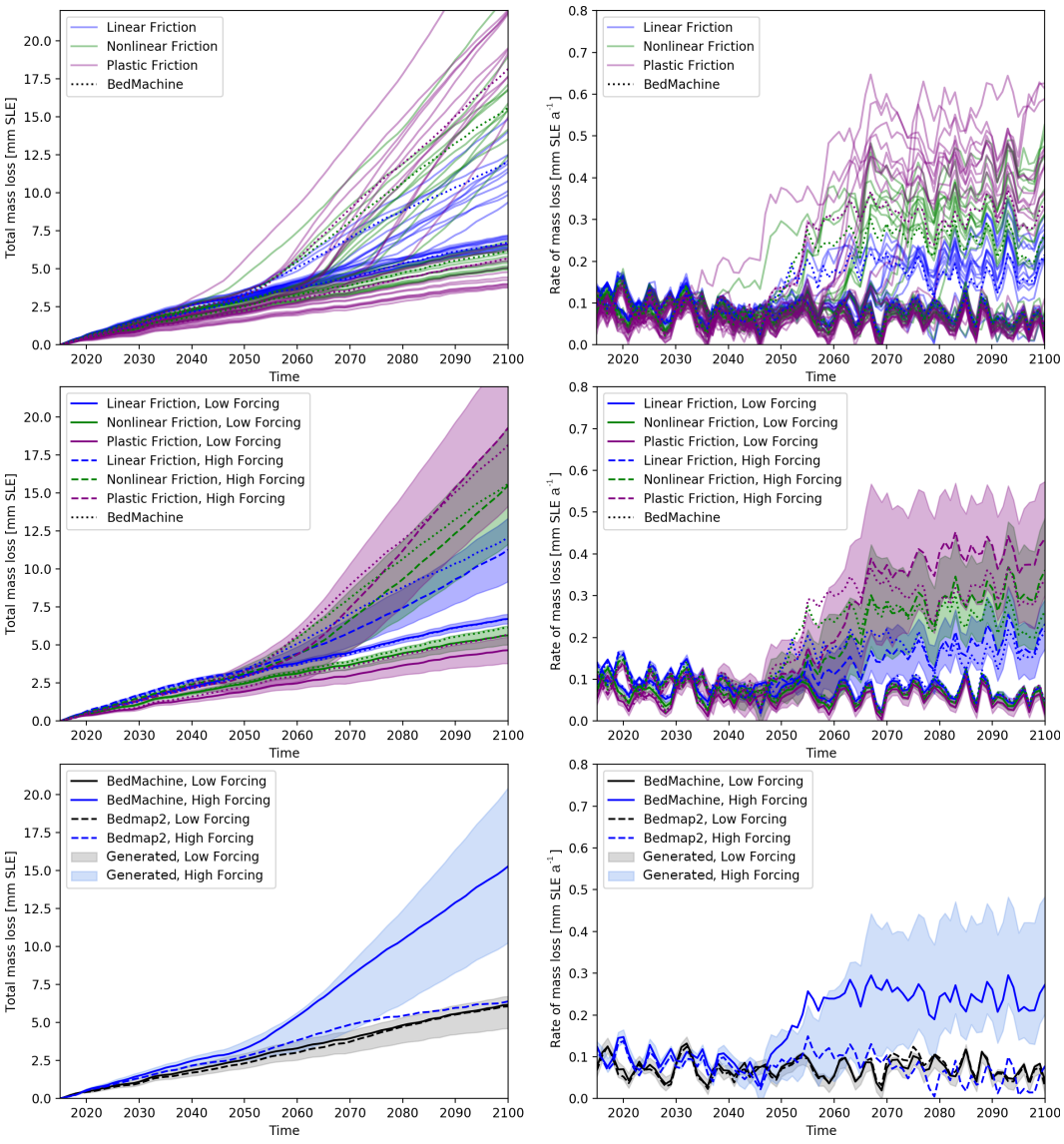

Figure 3. Net sea level contribution (left) and yearly rate (right). Individual simulations (top), grouped by friction law and forcing (middle) and grouped only by forcing including Bedmap2 (bottom). Shades correspond to ± one standard deviation.

Table 1. Mean 2100 sea level contribution estimates (relative to 2015) with one standard deviation of the statistically generated bedrock ensemble (both in mm SLE)

Friction law:	Linear	Nonlinear	Plastic
High Forcing:	11.3 ±2.08	15.5 ±3.86	19.4 ±5.15
Low Forcing:	6.7 ±0.31	5.6 ±0.62	4.7 ±0.87

contributions. This can be traced back to the slowdown of the ice as shown in Figure 2. Highly nonlinear friction laws facilitate decelerating ice to slow down even more and accelerating ice to speed up more than linear counterparts. This also explains why the predictive uncertainty due to the bedrock uncertainty strongly increases with non-linearity of the friction law and with stronger forcing. The standard deviation (STD) of the net sea level contribution over the 85 years increases with non-linearity (Table 1) which is consistent with the literature (Nias et al., 2016). The STD values range from 0.31 mm SLE for low forcing and linear friction to 5.15 mm SLE for high forcing and plastic friction which corresponds to about 5% to 25% of total sea level contribution (Figure 3 middle and Table 1).

All simulations shown here agree regarding the total sea level contribution for the low forcing scenario. However, with high forcing Bedmap2 runs are not consistent with the behaviour of simulations based on topographies generated here or BedMachine. For Bedmap2 simulations sea level rise contributions remain in the more stable, steadily evolving state regardless of forcing and friction law (Figure 3 bottom).

5 Discussion

The nonlinear response of PIG to strong forcing materializing in two distinct states is consistent with literature (Sun et al., 2014; Durand et al., 2011; Nias et al., 2018) and is in general agreement with the MISI hypothesis. None of these studies is designed to fully represent the current observational uncertainty in bedrock topography. Marine ice-cliff instability is not represented here but cannot be ruled out on these timescales. More research is needed to robustly represent marine ice-cliff instability in a well constrained way to predict how strong its impact would be on our simulations (Edwards et al., 2019).

Bedmap2 PIG simulations show less sensitivity to strong climate forcing than the statistically generated topographies and BedMachine but it is unclear what aspect of the topographies cause this response in the simulations: BedMachine uses a mass conservation approach where topographies are relaxed to avoid large mass flux divergence from inconsistent ice geometry-velocity combinations. Nias et al. (2018) supports our results in finding that a topography generated by a similar process to BedMachine exhibits a step change in mass loss which does not appear in Bedmap2 simulations. However, the topographies generated here, in common with Bedmap2, do not enforce a mass-conservation condition, share a topographic high near the Bedmap2 GL and use the same surface geometry. The fact that BedMachine does not share these characteristics, nor the same initial grounding line location, makes it even more remarkable that simulations using BedMachine and topographies generated here show consistent sea level rise contributions for both forcings. Our topographies show considerably more spatial variability in the topography than the relatively smooth Bedmap2 and BedMachine.

There are sporadic locations, including one about 20 km upstream of the BedMachine GL, where Bedmap2 topography is higher than all statistically generated topography and BedMachine (location highlighted in Figure 2, Figure S5 and Figure

S6 in the Supplement). Especially since this location is a local topographic low (Figure 2) it is not clear whether it can explain the unique behaviour of Bedmap2 (see also Text S5 in the Supplement). It is therefore unclear whether this behaviour is unique to PIG but we have been able to show that ice sheet simulations can generally be very sensitive to the bedrock topography. Whatever the exact reason, the striking underestimation of PIG mass loss for Bedmap2 simulations and high forcing relative to the other topographies (Figure 3, bottom), calls for caution in interpreting modelling projections of grounding line retreat obtained with this topography.

A limitation of our simulations is the resolution of statistically generated topographies of 4 km $\times$ 4 km (which is interpolated up to 500 m resolution within the adaptive grid refinement of BISICLES). The reason is the relatively high computational demand of a Cholesky decomposition which is used to generate random samples from a large covariance matrix. Evaluations of the mean field ('best estimate') would have been possible on fine resolutions, but would not have covered all of the uncertainties. The statistically generated topographies contain much more variability than both reference topographies and finer resolutions would, if anything, amplify this property. Nevertheless, simulations using Bedmap2 topography at 1 km resolution behave very similarly to those with degraded 4 km resolution (not shown).

To represent bedrock uncertainty in future simulations it would be desirable to have a set of topographies similar to the ones generated here but for more general setups, ideally continent-wide. This would allow different modelling groups to represent topographic uncertainty in predictions while retaining comparability. Similar approaches could be used to assess the value of additional measurements, e.g. for planning future campaigns.

In conclusion, we have been able to couple the representation of the topographic uncertainty in ice sheet simulations closely to observational constraints and demonstrate how this uncertainty interacts with other model parameters. The predictive uncertainty increases with non-linearity of the friction law and with higher melt forcing. One standard deviation can contribute between 5% and about 25% (equivalent to 5 mm SLE) of the 85-year signal, solely due to uncertainties in topography measurements and interpolation. These predictive uncertainties have been known to exist but until now remained largely omitted and unquantified. The low forcing scenario, which is more likely to be realized in very low greenhouse gas emission scenarios, would limit the PIG contribution to global mean sea level in this century. In addition we find the use of Bedmap2 to be likely to lead to an underestimation of the dynamic response of PIG to high forcing scenarios compared to the use of topographies designed explicitly to span the range of uncertainty which all suggest higher rates of mass loss.

6 Open Research

The simulations and bedrock topographies generated here are in public archive at Wernecke et al. (2021a),Wernecke et al. (2021b) and Wernecke et al. (2021c) (linear, nonlinear and plastic friction, respectively). Radio echo sounding data is available from Paden et al. (2010) and Holt, Blankenship, Corr, et al. (2006). The Python code for the statistical modelling of the representative topographies can be found at Wernecke (2021).

Acknowledgments
We would like to thank Jonty Rougier for inspirational discussions on this project. AW was supported by The Open University through a scholarship at the time of conducting this research. We acknowledge the support of the University of Bristol Advanced Computing Research Centre in providing computational resources for the

BISICLES simulations and the authors of Holt, Blankenship, Corr, et al. (2006) to provide us with an ungridded version of the data.

References

Agosta, C., Fettweis, X., & Datta, R. (2015). Evaluation of the cmip5 models in the aim of regional modelling of the antarctic surface mass balance. *The Cryosphere*, *9*, 2311–2321.

Alevropoulos-Borrill, A. V., Nias, I. J., Payne, A. J., Golledge, N. R., & Bingham, R. J. (2020). Ocean-forced evolution of the amundsen sea catchment, west antarctica, by 2100. *The Cryosphere*, *14*, 1245–1258.

Alley, R. B., Anandakrishnan, S., Christianson, K., Horgan, H. J., Muto, A., Parizek, B. R., ... Walker, R. T. (2015). Oceanic forcing of ice-sheet retreat: West antarctica and more. *Annual Review of Earth and Planetary Sciences*, *43*, 207–231.

Bamber, J. L., & Dawson, G. J. (2020). Complex evolving patterns of mass loss from antarctica's largest glacier. *Nature Geoscience*, *13*(2), 127–131.

Bamber, J. L., Westaway, R. M., Marzeion, B., & Wouters, B. (2018). The land ice contribution to sea level during the satellite era. *Environmental Research Letters*, *13*(6), 063008. doi: 10.1088/1748-9326/aac2f0

Barthel, A., Agosta, C., Little, C. M., Hattermann, T., Jourdain, N. N., Goelzer, H., ... Bracegirdle, T. T. (2020). Cmip5 model selection for ismip6 ice sheet model forcing: Greenland and antarctica. *The Cryosphere*, *14*(3), 855–879.

Bentsen, M., Bethke, I., Debernard, J. B., Iversen, T., Kirkevåg, A., Seland, Ø., ... others (2013). The norwegian earth system model, noresm1-m–part 1: description and basic evaluation of the physical climate. *Geoscientific Model Development*, *6*(3), 687–720.

Cornford, S. L., Martin, D., Payne, A., Ng, E., Le Brocq, A., Gladstone, R., ... Vaughan, D. G. (2015). Century-scale simulations of the response of the west antarctic ice sheet to a warming climate. *The Cryosphere*, *9*, 1579–1600. doi: 10.5194/tc-9-1579-2015

Cornford, S. L., Martin, D. F., Graves, D. T., Ranken, D. F., Le Brocq, A. M., Gladstone, R. M., ... Lipscomb, W. H. (2013). Adaptive mesh, finite volume modeling of marine ice sheets. *Journal of Computational Physics*, *232*(1), 529–549. doi: 10.1016/j.jcp.2012.08.037

Durand, G., Gagliardini, O., Favier, L., Zwinger, T., & Le Meur, E. (2011). Impact of bedrock description on modeling ice sheet dynamics. *Geophysical Research Letters*, *38*(20), L20501. doi: 10.1029/2011GL048892

Dutrieux, P., De Rydt, J., Jenkins, A., Holland, P. R., Ha, H. K., Lee, S. H., ... Schröder, M. (2014). Strong sensitivity of pine island ice-shelf melting to climatic variability. *Science*, *343*(6167), 174–178.

Edwards, T. L., Brandon, M. A., Durand, G., Edwards, N. R., Golledge, N. R., Holden, P. B., ... Wernecke, A. (2019). Revisiting antarctic ice loss due to marine ice-cliff instability. *Nature*, *566*(7742), 58–64. doi: 10.1038/s41586-019-0901-4

Favier, L., Durand, G., Cornford, S. L., Gudmundsson, G. H., Gagliardini, O., Gillet-Chaulet, F., ... Le Brocq, A. M. (2014). Retreat of pine island glacier controlled by marine ice-sheet instability. *Nature Climate Change*, *4*(2), 117–121. doi: 10.1038/nclimate2094

Favier, L., Jourdain, N. C., Jenkins, A., Merino, N., Durand, G., Gagliardini, O., ... Mathiot, P. (2019). Assessment of sub-shelf melting parameterisations using the ocean–ice-sheet coupled model nemo (v3. 6)–elmer/ice (v8. 3). *Geoscientific Model Development*, *12*(6), 2255–2283.

Fretwell, P., Pritchard, H. D., Vaughan, D. G., Bamber, J., Barrand, N., Bell, R., ... others (2013). Bedmap2: improved ice bed, surface and thickness datasets for

antarctica. *The Cryosphere*, *7*, 375–393. doi: 10.5194/tc-7-375-2013

Gasson, E., DeConto, R., & Pollard, D. (2015). Antarctic bedrock topography uncertainty and ice sheet stability. *Geophysical Research Letters*, *42*(13), 5372–5377.

Gladstone, R. M., Lee, V., Rougier, J., Payne, A. J., Hellmer, H., Le Brocq, A., ... Cornford, S. L. (2012). Calibrated prediction of pine island glacier retreat during the 21st and 22nd centuries with a coupled flowline model. *Earth and Planetary Science Letters*, *333*, 191–199. doi: 10.1016/j.epsl.2012.04.022

Holt, J. W., Blankenship, D. D., Corr, H. F., Morse, D. L., Vaughan, D. G., & Young, D. A. (2006). Subglacial topography: Airborne geophysical survey of the amundsen sea embayment, antarctica. from nov. 2004 to mar. 2005. U.S. Antarctic Program (USAP) Data Center. doi: 10.7265/N59W0CDC

Holt, J. W., Blankenship, D. D., Morse, D. L., Young, D. A., Peters, M. E., Kempf, S. D., ... Corr, H. F. (2006). New boundary conditions for the west antarctic ice sheet: Subglacial topography of the thwaites and smith glacier catchments. *Geophysical Research Letters*, *33*(9), L09502. doi: 10.1029/2005GL025561

Joughin, I., & Alley, R. B. (2011). Stability of the west antarctic ice sheet in a warming world. *Nature Geoscience*, *4*(8), 506–513.

Joughin, I., Smith, B. E., & Medley, B. (2014). Marine ice sheet collapse potentially under way for the thwaites glacier basin, west antarctica. *Science*, *344*(6185), 735–738. doi: 10.1126/science.1249055

Joughin, I., Smith, B. E., & Schoof, C. G. (2019). Regularized coulomb friction laws for ice sheet sliding: Application to pine island glacier, antarctica. *Geophysical Research Letters*, *46*(9), 4764–4771. doi: 10.1029/2019GL082526

Jourdain, N. C., Asay-Davis, X., Hattermann, T., Straneo, F., Seroussi, H., Little, C. M., & Nowicki, S. (2020). A protocol for calculating basal melt rates in the ismip6 antarctic ice sheet projections. *The Cryosphere*, *14*(9), 3111–3134.

Milillo, P., Rignot, E., Mouginot, J., Scheuchl, B., Morlighem, M., Li, X., & Salzer, J. T. (2017). On the short-term grounding zone dynamics of pine island glacier, west antarctica, observed with cosmo-skymed interferometric data. *Geophysical Research Letters*, *44*(20), 10–436.

Morlighem, M. (2019). Measures bedmachine antarctica, version 1. Boulder, Colorado USA. NASA National Snow and Ice Data Center Distributed Active Archive Center. (Accessed: 2020-02) doi: 10.5067/C2GFER6PTOS4

Morlighem, M., Rignot, E., Binder, T., Blankenship, D., Drews, R., Eagles, G., ... others (2020). Deep glacial troughs and stabilizing ridges unveiled beneath the margins of the antarctic ice sheet. *Nature Geoscience*, *13*(2), 132–137. doi: 10.1038/s41561-019-0510-8

Mouginot, J., Rignot, E., & Scheuchl, B. (2014). Sustained increase in ice discharge from the amundsen sea embayment, west antarctica, from 1973 to 2013. *Geophysical Research Letters*, *41*(5), 1576–1584.

Mouginot, J., Scheuchl, B., & Rignot, E. (2017). Measures antarctic boundaries for ipy 2007-2009 from satellite radar, version 2. Boulder, Colorado USA. NASA National Snow and Ice Data Center Distributed Active Archive Center. (Accessed: 2019-07) doi: 10.5067/AXE4121732AD

Naughten, K. A., Meissner, K. J., Galton-Fenzi, B. K., England, M. H., Timmermann, R., & Hellmer, H. H. (2018). Future projections of antarctic ice shelf melting based on cmip5 scenarios. *Journal of Climate*, *31*(13), 5243–5261.

Nias, I. J., Cornford, S., & Payne, A. (2018). New mass-conserving bedrock topography for pine island glacier impacts simulated decadal rates of mass loss. *Geophysical Research Letters*, *45*(7), 3173–3181. doi: 10.1002/2017GL076493

Nias, I. J., Cornford, S. L., & Payne, A. J. (2016). Contrasting the modelled sensitivity of the amundsen sea embayment ice streams. *Journal of Glaciology*, *62*(233), 552–562. doi: 10.1017/jog.2016.40

Oppenheimer, M., Glavovic, B., Hinkel, J., van de Wal, R., Magnan, A. K., Abd-

Elgawad, A., ... Sebesvari, Z. (2019). Sea level rise and implications for low lying islands, coasts and communities. In *Ipcc special report on the ocean and cryosphere in a changing climate [h.-o. portner, d.c. roberts, v. masson-delmotte, p. zhai, m. tignor, e. poloczanska, k. mintenbeck, a. alegria, m. nicolai, a. okem, j. petzold, b. rama, n.m. weyer (eds.)]*. The Intergovernmental Panel on Climate Change.

Paden, J., Li, J., Leuschen, C., Rodriguez-Morales, F., & Hale, R. (2010). Icebridge mcords l2 ice thickness, version 1. from oct. 2009 to dec. 2017. Boulder, Colorado USA. NASA National Snow and Ice Data Center Distributed Active Archive Center. (updated 2019, Accessed: 2019-09) doi: 10.5067/GDQ0CUCVTE2Q

Rasmussen, C. E., & Williams, C. K. (2006). *Gaussian processes for machine learning* (Vol. 2) (No. 3). MIT Press Cambridge, MA.

Rignot, E., Bamber, J. L., Van Den Broeke, M. R., Davis, C., Li, Y., Van De Berg, W. J., & Van Meijgaard, E. (2008). Recent antarctic ice mass loss from radar interferometry and regional climate modelling. *Nature Geoscience*, *1*(2), 106–110. doi: 10.1038/ngeo102

Rignot, E., Jacobs, S., Mouginot, J., & Scheuchl, B. (2013). Ice-shelf melting around antarctica. *Science*, *341*(6143), 266–270.

Rignot, E., Mouginot, J., Morlighem, M., Seroussi, H., & Scheuchl, B. (2014). Widespread, rapid grounding line retreat of pine island, thwaites, smith, and kohler glaciers, west antarctica, from 1992 to 2011. *Geophysical Research Letters*, *41*(10), 3502–3509. doi: 10.1002/2014GL060140

Rignot, E., Mouginot, J., & Scheuchl, B. (2017). Measures insar-based antarctica ice velocity map, version 2. Boulder, Colorado USA. NASA National Snow and Ice Data Center Distributed Active Archive Center. (Accessed: 2018-11) doi: 10.5067/D7GK8F5J8M8R

Rignot, E., Velicogna, I., van den Broeke, M. R., Monaghan, A., & Lenaerts, J. T. (2011). Acceleration of the contribution of the greenland and antarctic ice sheets to sea level rise. *Geophysical Research Letters*, *38*(5), L05503. doi: 10.1029/2011GL046583

Schlegel, N.-J., Seroussi, H., Schodlok, M. P., Larour, E. Y., Boening, C., Limonadi, D., ... Broeke, M. R. (2018). Exploration of antarctic ice sheet 100-year contribution to sea level rise and associated model uncertainties using the issm framework. *The Cryosphere*, *12*(11), 3511–3534. doi: 10.5194/tc-12-3511-2018

Schoof, C. (2007). Ice sheet grounding line dynamics: Steady states, stability, and hysteresis. *Journal of Geophysical Research: Earth Surface*, *112*(F3), F03S28.

Schoof, C., & Hindmarsh, R. C. (2010). Thin-film flows with wall slip: an asymptotic analysis of higher order glacier flow models. *Quarterly Journal of Mechanics and Applied Mathematics*, *63*(1), 73–114. doi: 10.1093/qjmam/hbp025

Seroussi, H., Nowicki, S., Payne, A. J., Goelzer, H., Lipscomb, W. H., Abe Ouchi, A., ... Zwinger, T. (2020). Ismip6 antarctica: a multi-model ensemble of the antarctic ice sheet evolution over the 21st century. *The Cryosphere*. doi: 10.5194/tc-14-3033-2020

Shepherd, A., Ivins, E., Rignot, E., Smith, B., Van Den Broeke, M., Velicogna, I., ... Wouters, B. (2018). Mass balance of the antarctic ice sheet from 1992 to 2017. *Nature*, *558*, 219–222. doi: 10.1038/s41586-018-0179-y

Sun, S., Cornford, S., Liu, Y., & Moore, J. C. (2014). Dynamic response of antarctic ice shelves to bedrock uncertainty. *The Cryosphere*, *8*(4), 1561–1576.

Wernecke, A. (2020). *Quantifying century-scale uncertainties of the global mean sea level rise contribution from the amundsen sea sector, west antarctica* (Doctoral dissertation, The Open University). doi: 10.21954/ou.ro.0001223d

Wernecke, A. (2021, December). *script to generate stat. samples of PIG topography*

with Gaussian Process model. Zenodo. Retrieved from https://doi.org/10.5281/zenodo.5788669 doi: 10.5281/zenodo.5788669

Wernecke, A., Tamsin, L., Edwards, Holden, B., Philip, Edwards, N. R., & Cornford, S. L. (2021a, October). *BISICLES Pine Island Glacier simulations with linear friction.* Zenodo. Retrieved from https://doi.org/10.5281/zenodo.5553288 doi: 10.5281/zenodo.5553288

Wernecke, A., Tamsin, L., Edwards, Holden, B., Philip, Edwards, N. R., & Cornford, S. L. (2021b, October). *BISICLES Pine Island Glacier simulations with nonlinear friction.* Zenodo. Retrieved from https://doi.org/10.5281/zenodo.5553311 doi: 10.5281/zenodo.5553311

Wernecke, A., Tamsin, L., Edwards, Holden, B., Philip, Edwards, N. R., & Cornford, S. L. (2021c, October). *BISICLES Pine Island Glacier simulations with strongly nonlinear friction.* Zenodo. Retrieved from https://doi.org/10.5281/zenodo.5553320 doi: 10.5281/zenodo.5553320

Zhao, C., Gladstone, R. M., Warner, R. C., King, M. A., Zwinger, T., & Morlighem, M. (2018). Basal friction of fleming glacier, antarctica–part 1: Sensitivity of inversion to temperature and bedrock uncertainty. *The Cryosphere*, *12*(8), 2637–2652.